

Spectral-Adaptive Modulation Networks for Visual Perception

Guhnoo Yun, *Student Member, IEEE*, Juhan Yoo, Kijung Kim, Jeongho Lee,
Paul Hongsuck Seo, Dong Hwan Kim, *Member, IEEE*

Abstract—Recent studies have shown that 2D convolution and self-attention exhibit distinct spectral behaviors, and optimizing their spectral properties can enhance vision model performance. However, theoretical analyses remain limited in explaining why 2D convolution is more effective in high-pass filtering than self-attention and why larger kernels favor shape bias, akin to self-attention. In this paper, we employ graph spectral analysis to theoretically simulate and compare the frequency responses of 2D convolution and self-attention within a unified framework. Our results corroborate previous empirical findings and reveal that node connectivity, modulated by window size, is a key factor in shaping spectral functions. Leveraging this insight, we introduce a *spectral-adaptive modulation* (SPAM) mixer, which processes visual features in a spectral-adaptive manner using multi-scale convolutional kernels and a spectral re-scaling mechanism to refine spectral components. Based on SPAM, we develop SPANetV2 as a novel vision backbone. Extensive experiments demonstrate that SPANetV2 outperforms state-of-the-art models across multiple vision tasks, including ImageNet-1K classification, COCO object detection, and ADE20K semantic segmentation.

Index Terms—SPANetV2, deep learning, visual perception, convolution, self-attention, spectral-adaptive modulation, neural networks.

I. INTRODUCTION

Developing powerful backbone architectures is important in computer vision, and Convolutional Neural Networks (CNNs) have long been the predominant approach for addressing a wide range of vision tasks, due to their strong inductive bias in capturing local information [1]–[4]. Over the last few years, however, with the success of Vision Transformer (ViT) [5], many follow-up models based on the ViT paradigm have gained significant traction, and have become one of the dominant structures as an alternative to CNNs in various computer vision tasks including image classification [6]–[9], object detection [10]–[12], segmentation [13], [14], and beyond [15]–[18]. The primary reason for ViT’s success lies in the self-attention mechanism, which effectively captures long-range dependencies without relying on a strong inductive bias [5], [19]–[23]. This widely accepted notion has prompted

the development of numerous variants of self-attention, aimed at further improving the performance of ViT-based models [6], [8], [24]–[26].

Following the success of ViTs, many researchers expected Transformers to dominate computer vision. However, recent studies challenge this view, demonstrating competitive performance without self-attention mechanisms. Notably, Multi-Layer Perceptron (MLP)-based approaches [27]–[31] have shown promising results in vision tasks, narrowing the performance gap between MLP-based models and ViTs. Beyond MLPs, various methods have also emerged as effective alternatives to self-attention. For instance, Fast Fourier Transform (FFT)-based models [32]–[34] have demonstrated feasibility as self-attention substitutes. Similarly, graph convolution [35] and clustering-based token-mixers [36], [37] have been effectively employed to encode image patches. These approaches highlight that self-attention is not the sole dominant method for spatial patch modulation. Instead, diverse techniques can enhance vision backbones.

Concurrently, CNN research has evolved by integrating strategies inspired by ViTs, revitalizing its significance. ResNet Strikes Back [38] demonstrated that applying advanced training techniques from ViTs, such as those in DeiT [6] and Swin Transformer [8], improves ResNet-50 performance by 2.3%. Similarly, ConvNeXt [39] incorporated design elements from Swin models [8], showing that CNNs can rival ViTs by adopting larger kernels and advanced block modules. Numerous other studies further support these findings [40]–[45].

Several studies have explored the fundamental differences between self-attention and convolution [5], [20]–[22], leveraging their distinct advantages [46]–[50]. Recent research has moved beyond inductive bias analysis to evaluating effectiveness in the spectral domain. A common finding [51]–[55] is that self-attention acts as a low-pass filter, whereas convolution effectively captures high-frequency components. Notably, Wang *et al.* [53] proposed a framework that explains why self-attention behaves as a low-pass filter in the Fourier domain. In contrast, the spectral properties of CNNs have primarily been examined through empirical observations [51], [52], [54], [56]. Thus, a theoretical framework is needed to characterize the origins of these spectral differences.

To address this, we draw inspiration from kernel size effects. Ding *et al.* [40] argue that large kernel design expands effective receptive fields (ERFs) and favors shape bias, akin to self-attention. Intuitively, enlarging 2D convolution kernels broadens spatial interactions between patches, analogous to ex-

Manuscript received Month Day, Year; revised Month Day, Year.

Guhnoo Yun, Kijung Kim, Jeongho Lee, and Dong Hwan Kim are with Korea University (KU) in Seoul, Korea, and Korea Institute of Science and Technology (KIST) in Seoul, Korea. (e-mail: {doranlyong, plan100day, kape67, gregorykim}@kist.re.kr).

Juhan Yoo is with Dong-A University in Busan, Korea (e-mail: uncho-into@dau.ac.kr).

Paul Hongsuck Seo is with Korea University in Seoul, Korea (e-mail: phseo@korea.ac.kr).

Corresponding author: Dong Hwan Kim (e-mail: gregorykim@kist.re.kr).

Our code is available at <https://github.com/DoranLyong/SPANetV2-official>.

panding node connectivity in graphs. In contrast, self-attention can be represented as a fully connected graph, where patches act as nodes and attention weights define edges representing their interactions. Given these perspectives, we adopt a graph-based framework to represent both 2D convolution and self-attention in Euclidean space and analyze them using graph spectral analysis. As a result, we theoretically find that *large-kernel convolution functions as a low-pass filter, akin to self-attention, whereas small-kernel convolution inherently filters both low- and mid/high-frequency components.*

Building on these findings, we propose a novel token mixer, *Spectral-Adaptive Modulation (SPAM)*, for image feature aggregation. In our previous work [57], it was demonstrated that *optimally aggregating spectral components of image patches enhances the performance of vision models.* Building on this idea, our new SPAM encodes image patches in a spectral-adaptive manner by employing convolutions with multiple kernel sizes and applying frequency-domain mask filtering to modulate spectral characteristics. Furthermore, we introduce *SPANetV2*, incorporating SPAM within the MetaFormer architecture [45]. SPANetV2 is evaluated on multiple vision tasks, including image classification, object detection, and semantic segmentation, achieving superior performance over previous state-of-the-art models.

Our contributions are threefold. (1) We theoretically analyze convolution and self-attention through graph signal processing, providing a unified framework for spectral analysis from a graph perspective. This view enables a comprehensive comparison of their spectral properties, explaining why small-kernel designs are more adept at high-pass filtering, whereas large-kernel designs favor low-pass filtering, akin to self-attention, corroborating previous experimental findings [40], [51], [52], [54]. (2) Building on our previous work, we propose SPAM, a novel token-mixer for spectral-adaptive image feature aggregation, leveraging multi-kernel convolutions and frequency-domain filtering. We then introduce SPANetV2, a new vision architecture that incorporates SPAM. (3) Our SPANetV2 is evaluated on multiple vision tasks, including image classification [58], object detection [59], and semantic segmentation [60]. Our results demonstrate that SPANetV2 outperforms state-of-the-art models.

II. RELATED WORKS

A. CNNs, ViTs, and Beyond for Vision Architecture

CNNs [1]–[4] predominated vision tasks until the emergence of Transformers [61], initially designed to capture long-range dependencies in language tasks via self-attention. Inspired by their success, Transformers were introduced into vision by ViT [5], achieving remarkable performance in image classification. Subsequent studies have improved ViT’s self-attention mechanisms using various approaches, including shifted windows [8], relative positional encoding [62], anti-aliasing attention [63], and convolution integration [7], [64], [65].

While self-attention is widely considered crucial for ViT performance, several studies have questioned its necessity. For instance, fully replacing self-attention with MLP-based mixers

can yield competitive results [27], [29]. These findings have prompted further exploration of alternative token mixers [28], [66], challenging attention dominance through various non-attention approaches [32]–[37], [67], [68].

Several other studies have explored transformer architectures within meta-architectures by replacing self-attention with non-parametric token mixers. For example, ShiftViT [69] employs a partial shift operation [70], and PoolFormer [45], [71] utilizes spatial average pooling. Both achieve competitive performance across various vision tasks, highlighting the effectiveness of meta-architecture block and stage designs. Following these, we adopt the MetaFormer architecture [45], replacing the token mixer with our proposed SPAM.

B. Frequency in Images

In computer vision literature, images have been extensively studied in the spectral domain. Normally, low frequencies encode global structures and color information, while high frequencies capture fine details (*e.g.*, local edges/textures) [72]–[74]. Several studies [51]–[55] indicate that self-attention predominantly captures low-frequency representations but struggles with high-frequency information. In contrast, convolution exhibits the opposite trend. Consistent with these findings, several works [33], [34], [50], [52], [57], [75] show that optimizing frequency components for feature aggregation enhances vision model performance.

Wang *et al.* [53] proposed a theoretical framework for analyzing ViT features in the Fourier domain. However, to the best of our knowledge, the spectral properties of convolutions in CNNs have primarily been examined through empirical methods, such as spectral noise testing [52], [54], [56] and observation of spectral components [51] in pre-trained models. In this paper, we address this gap by introducing a unified framework using graph spectral analysis. Since images can be represented as grid-structured graphs, they can be analyzed from a graph perspective.

C. Frequency in Graphs

Graph signal processing (GSP) theory [76] extends signal processing to graph-based data, employing the graph Fourier transform (GFT) to analyze and manipulate signals on irregular structures. By leveraging graph topology, GSP provides powerful tools for applications such as network analysis and image processing. Balcilar *et al.* [77] proposed a theoretical framework for understanding graph neural networks (GNNs) through frequency response analysis.

Building on this framework, we analyze how convolutional kernels of varying sizes capture spectral components, offering theoretical insights into the spectral differences between convolution and self-attention. Additionally, we explain why larger kernels favor shape bias, akin to self-attention in vision tasks [40]. Expanding on this analysis, we propose the SPAM mixer for spectral-adaptive visual feature aggregation and introduce SPANetV2 as a new vision backbone.

III. SPECTRAL ANALYSIS IN A GRAPH FORMULATION

This section compares 2D convolution in CNNs with self-attention in ViTs through spectral analysis via graph spectral filtering [76]–[78]. Balcilar *et al.* [77] proposed a framework that generalizes non-Euclidean graph convolution, 2D Euclidean convolution, and graph attention. Modeling images as a regular grid graph allows convolution and self-attention to be reformulated within this framework, enabling their spectral comparison.

A. Background

1) *Spectral filtering in graphs.*: Let G represent an undirected graph consisting of N nodes and a variable number of edges. The structural properties of the graph are given by the adjacency matrix $A \in \{0, 1\}^{N \times N}$, and the normalized graph Laplacian L can be defined as $L = I - D^{-1/2}AD^{-1/2}$. Here, $D \in \mathbb{R}^{N \times N}$ is the diagonal degree matrix and I is the identity matrix. L can be expressed using eigendecomposition as $L = U \text{diag}(\lambda) U^T$, where $U \in \mathbb{R}^{N \times N}$ denotes a matrix whose columns are the eigenvectors. $\text{diag}(\lambda)$ generates a diagonal matrix whose diagonal components are derived from the elements of eigenvalues $\lambda \in \mathbb{R}^N$. Since L is a real symmetric matrix, it has a complete set of orthonormal eigenvectors, and its eigenvalues are constrained to the range between 0 and 2 [78]. In graph signal processing theory [76], graph signals can be filtered in the spectral domain by utilizing the eigenvectors of the normalized graph Laplacian matrix as the bases in GFT. Given a signal $\mathbf{h} \in \mathbb{R}^N$, the GFT is defined as $\hat{\mathbf{h}} = U^T \mathbf{h}$, and the inverse GFT (iGFT) is $\mathbf{h} = U \hat{\mathbf{h}}$. Then, the convolution $*$ between the signal \mathbf{h} and convolution kernel \mathbf{f} is described as follows:

$$\mathbf{f} * \mathbf{h} = U((U^T \mathbf{f}) \odot (U^T \mathbf{h})) = U \text{diag}(\Phi(\lambda)) U^T \mathbf{h}, \quad (1)$$

where \odot denotes the element-wise product, $\Phi(\cdot)$ is the desired filter function, and $\text{diag}(\Phi(\lambda))$ represents the convolution kernel in the spectral domain.

2) *Frequency response of GNNs*: GNN operation involves two steps: aggregating neighborhood nodes and updating through linear transformation. For spatial GNNs, they can be generalized as propagating node features to neighboring nodes [77], as shown below:

$$H^{(l+1)} = \sigma\left(\sum_{i=1}^{N_f} C^{(i)} H^{(l)} W^{(l,i)}\right), \quad (2)$$

where σ is an activation function, N_f is the number of filters, $C^{(i)} \in \mathbb{R}^{N \times N}$ is a convolution support for the i -th filter that defines how the node features are propagated to neighborhood nodes, $H \in \mathbb{R}^{N \times d_l}$ is a set of N node features with d dimensions, and $W^{(l,i)} \in \mathbb{R}^{d_l \times d_{l+1}}$ is a trainable matrix for the i -th filter of the l -th layer. Spectral GNNs work all the same way as spatial GNNs, but are defined using a function of eigenvalues $\Phi_i(\lambda)$ and eigenvectors U of the normalized graph Laplacian L . Specifically, $C^{(i)}$ can be interpreted in the spectral domain and is derived by $U \text{diag}(\Phi_i(\lambda)) U^T$ [77]. So, the frequency response of $C^{(i)}$ is defined as:

$$\Phi_i(\lambda) = \text{diag}^{-1}(U^T C^{(i)} U), \quad (3)$$

where $\text{diag}^{-1}(\cdot)$ returns the vector consisting of the diagonal elements of the given matrix.

B. Graph Formulation for Convolution and Self-Attention

The 1D sequential inputs of ViTs and the 2D regular grid inputs of CNNs are special cases of graphs. Thus, both convolution and self-attention can be analyzed within the GNN framework. For clarity, we define image features as $\tilde{X} \in \mathbb{R}^{D \times H \times W}$, where D , H , and W denote the number of feature dimensions, height, and width, respectively. The d -th feature is represented as $\tilde{X}_d \in \mathbb{R}^{H \times W}$.

1) *2D convolution using a sparse matrix*: A 2D Euclidean convolution with a kernel $\tilde{K} \in \mathbb{R}^{m \times m}$ is performed by sliding the kernel over an image feature \tilde{X}_d , applying element-wise multiplication to each grid patch, and summing the results to generate the output feature. This section formulates this operation as sparse matrix multiplication [79], [80], with a focus on constructing the sparse convolution support matrix $C^{(i)}$. For simplicity, we consider a single-channel 2D convolution and hence denote $C^{(i)}$ simply as C .

To formulate 2D convolution as a sparse matrix multiplication, we define a sparse matrix $C \in \mathbb{R}^{H_{out} W_{out} \times HW}$. Given the z -th kernel element located at position (r, t) in the kernel \tilde{K} , indexed using zero-based ordering as $z = r \times m + t$, the matrix C is constructed as a weighted sum of fixed basis convolution support matrices $B^{(z)} \in \{0, 1\}^{H_{out} W_{out} \times HW}$:

$$C = \sum_{z=0}^{Z-1} k^{(z)} B^{(z)}, \quad (4)$$

where $Z = m \times m$ and $k^{(z)} \in \mathbb{R}$ denotes the kernel value at index z . Each $B^{(z)}$ encodes the spatial relationship between the z -th kernel element position and the corresponding input positions across all sliding windows, accounting for zero-padding, by indicating which input elements are multiplied by the z -th kernel weight at each location. The output dimensions are defined as:

$$H_{out} = \left\lfloor \frac{H + 2p - m}{s} \right\rfloor + 1, \quad (5a)$$

$$W_{out} = \left\lfloor \frac{W + 2p - m}{s} \right\rfloor + 1, \quad (5b)$$

where $\lfloor \cdot \rfloor$ is the floor function, p is the padding size, m is the kernel size, and s is stride. We set $p = \lfloor (m - 1)/2 \rfloor$ and $s = 1$ to maintain the output size equal to the input size.

To construct the elements of $B^{(z)}$, we consider the position (r, t) of the z -th kernel element. For an output position (y, x) , the corresponding indices in the flattened output and input are computed as:

$$a = y \times W + x, \quad (6a)$$

$$b = (y + r - p) \times W + (x + t - p), \quad (6b)$$

where a and b denote the indices in the flattened output and input, respectively. The input index b is adjusted for

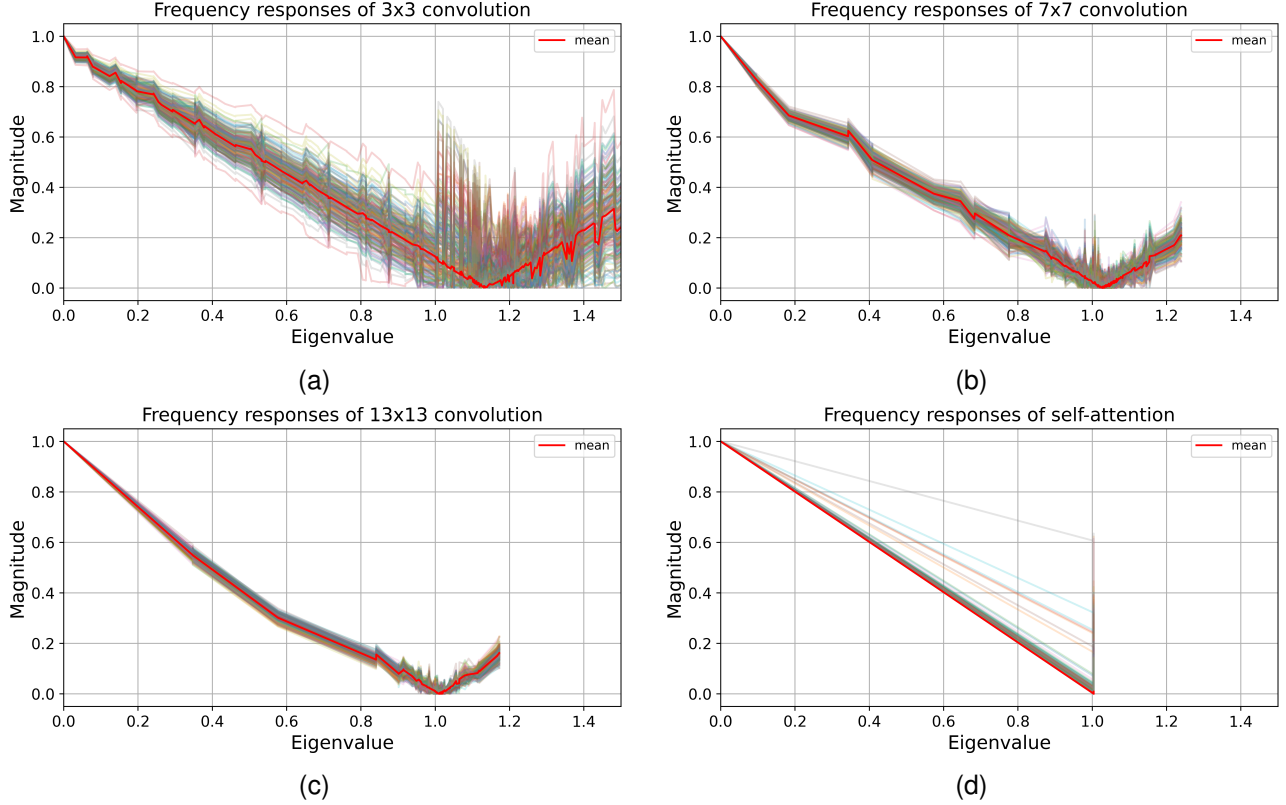


Fig. 1. **Simulation examples of frequency response.** (a)-(c) show responses of 2D Euclidean convolutions with increasing kernel sizes, and (d) shows responses of self-attention. All responses are obtained with random weights. The input patch size is set to 16×16 , inspired by ViT [5]. As the convolution kernel size increases, the cut-off frequency shifts closer to one, making it behave more like a low-pass filter, akin to self-attention.

padding and aligned with the corresponding kernel element. The elements of $B^{(z)}$ are then assigned as:

$$B_{a,b}^{(z)} = B_{a,b}^{(r,t)} = \begin{cases} 1 & \text{if } 0 \leq (y+r-p) < H \text{ and} \\ & 0 \leq (x+t-p) < W, \\ 0 & \text{otherwise.} \end{cases} \quad (7)$$

This condition ensures that $B^{(z)}$ correctly maps between the kernel element $k^{(z)}$ and the valid regions of the input feature. Specifically, $B_{a,b}^{(z)} = 1$ if the kernel element $k^{(z)}$ lies within the receptive field of \tilde{X}_d , including zero-padding; otherwise, $B_{a,b}^{(z)} = 0$. Thus, the 2D convolution operation is formulated as:

$$\tilde{X}_d \circledast \tilde{K} = CX_d = \sum_{z=0}^{Z-1} B^{(z)} X_d k^{(z)}, \quad (8)$$

where $X_d \in \mathbb{R}^{HW}$ represents the flattened \tilde{X}_d . For clarity and concise formulation, the reshaping step to align tensors on the left-hand and right-hand sides is omitted. This formulation represents 2D convolution as sparse matrix multiplication, emphasizing its relationship with the spatial structure of the input. For simplicity, the bias term is omitted. This sparse matrix representation enables frequency response analysis of 2D convolution by examining the properties of C , which directly stem from the convolution kernel \tilde{K} .

2) *Self-attention*: Self-attention in ViTs models relationships between patches, representing each patch as a node

in a fully connected graph. The connection strengths are determined by an attention weight matrix, computed from the query (Q) and key (K) matrices. Given $Q, K \in \mathbb{R}^{HW \times d_h}$, obtained by projecting $X \in \mathbb{R}^{D \times HW}$ with trainable weight matrices, the attention matrix $E \in \mathbb{R}^{HW \times HW}$ is defined as:

$$E = \text{softmax} \left(\frac{QK^T}{\sqrt{d_h}} \right), \quad (9)$$

where d_h denotes the head dimension, and softmax is applied along the last dimension to normalize attention scores.

The final attention mechanism is expressed as $E(X^T W_v) = EX^T W_v$, where $W_v \in \mathbb{R}^{D \times d_h}$ represents the value projection matrix. This can also be reformulated using convolution support matrices by defining $C^{(i)} \in \mathbb{R}^{HW \times HW}$ as the attention weights for each input patch pair. Unlike the binary values in Equation 7, $C^{(i)}$ contains continuous attention weights between query-key pairs:

$$C_{a,b}^{(i)} = \frac{\exp(Q_a K_b^T / \sqrt{d_h})}{\sum_{j=0}^{J-1} \exp(Q_a K_j^T / \sqrt{d_h})}, \quad (10)$$

where $C_{a,b}^{(i)} \in \mathbb{R}$ denotes the attention weight between the a -th query and b -th key, and $J = H \times W$. Consequently, self-attention can be rewritten as:

$$\text{Attention}(X) = E(X^T W_v) = \sum_{i=1}^{d_h} C^{(i)} X^T w_v^{(i)}, \quad (11)$$

where $w_v^{(i)} \in \mathbb{R}^{D \times d_h}$ is a sparse matrix with only its i -th column containing the corresponding column vector from W_v .

C. Frequency Response Profiling

1) *Simulation*: For straightforward profiling [77], we run 240 simulations with both randomly generated weights and 16×16 patches to estimate the expected frequency responses of $C^{(i)}$ for 2D convolution and self-attention. In 2D convolution, patch connections are dictated by the kernel size, forming a locally connected graph, whereas self-attention constructs a fully connected graph, linking all patches. Based on these properties, we construct adjacency matrices, compute their eigenvectors, and simulate frequency responses using Equation 3. Figure 1 shows the simulated frequency responses.

As can be seen, small kernels tend to filter both low- and slightly mid/high-frequency components, while larger kernels shift the cut-off frequency closer to one, functioning as low-pass filters similar to self-attention. This trend occurs because a larger receptive field averages out high-frequency components. Although these results are simulated rather than learned, they demonstrate distinct different spectral behaviors in convolution and self-attention, as observed in prior studies [51]–[55].

2) *Discussion*: The graph spectral profile range is determined by the node connectivity and computed via the eigendecomposition of the normalized graph Laplacian L . In 2D Euclidean convolution, image patches are represented as nodes in a grid graph, where connections are dictated by the kernel size. For example, regular 3×3 kernels link each node to its eight neighbors, resulting in a sparse adjacency matrix A that captures only local connections. Thus, L for the 2D convolution encodes the local structure of these connections. Following Equation 1, 2, and 8, the 2D Euclidean convolution operation is expressed in the graph spectral domain as:

$$\tilde{X}_d \circledast \tilde{K} = Uf(\Lambda)U^T X_d, \quad (12)$$

where $f(\Lambda)$ modifies the eigenvalues based on the kernel \tilde{K} , and Λ is a diagonal matrix whose diagonal components are eigenvalues of L .

Based on the simulation results in Figure 1, node connectivity can be considered a key factor in utilizing the spectral characteristics of convolution and self-attention. For instance, Swin Transformer [8] captures high-frequency signals more effectively than ViT [5] by employing the shifted window mechanism [57], which enhances local node connectivity in self-attention. Similarly, HiLo attention [81] uses a local window to improve high-frequency capture. Conversely, larger kernels increase global node connectivity, acting as low-pass filters. Low-frequency components encode global structures associated with shape bias [82], aligning with Ding *et al.* [40], who found that large kernel designs favor shape bias similar to self-attention. These insights suggest that adjusting kernel size can modulate spectral properties in convolutional operations. Furthermore, kernel size modulation can induce spectral functions akin to self-attention, and *vice versa*. In the next section, we introduce a novel convolutional mixer that

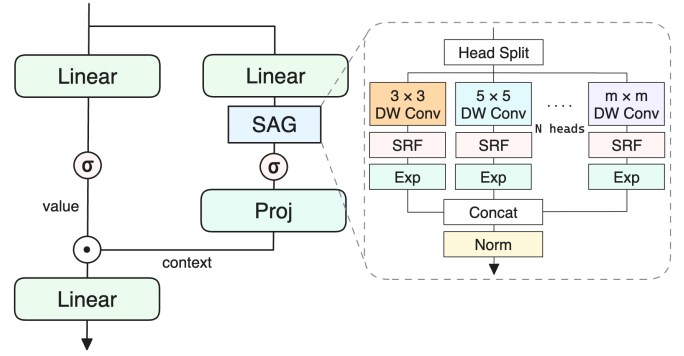


Fig. 2. **Overview of the SPAM mixer.** The *Head Split* layer evenly partitions the input along feature dimensions based on the number of heads. *DWConv* denotes depthwise convolution, while *SRF* re-scales the spectral components of *DWConv*'s output. All linear layers preserve input dimensions, except *Exp*, which doubles the feature dimensions, and *Proj*, which halves them.

aggregates visual features in a spectral-adaptive manner by leveraging this property.

IV. A SPECTRAL-ADAPTIVE TOKEN MIXER

From a spectral perspective, optimal aggregation of spectral components in image patches enhances vision model performance [57]. In this section, we propose a novel token mixer incorporating spectral-adaptive convolutional modulation.

A. Convolutional Modulation

Convolutional modulation [42], [57], [83] leverages convolution to mimic self-attention through a different way. This approach first aggregates contextual information, then modulates projected feature values via element-wise multiplication:

$$\tilde{Y} = \mathcal{V}(\tilde{X}) \odot \mathcal{C}(\tilde{X}), \quad (13)$$

where $\mathcal{V}(\tilde{X})$ represents projected feature values, $\mathcal{C}(\tilde{X})$ denotes aggregated contexts, and $\tilde{Y} \in \mathbb{R}^{D \times H \times W}$ is the refined representation. Here, $\mathcal{V}(\cdot)$ and $\mathcal{C}(\cdot)$ correspond to value projection and context aggregation functions, respectively. We define $\mathcal{V}(\cdot)$ as a non-linear transformation:

$$\mathcal{V}(\tilde{X}) = \sigma(\text{Linear}(\tilde{X})) \in \mathbb{R}^{D \times H \times W}, \quad (14)$$

where $\text{Linear}(\cdot)$ denotes a linear projection, and $\sigma(\cdot)$ represents an activation function. Next, we introduce $\mathcal{C}(\cdot)$ for spectral-adaptive context aggregation.

B. Spectral-Adaptive Context Aggregation

To achieve spectral-adaptive context aggregation, we introduce the *spectral-adaptive gate* (SAG), as illustrated in Figure 2. SAG comprise N heads to capture diverse spectral responses, with each head processing an evenly partitioned input segment of size $d_h = \frac{D}{N}$ along the feature dimensions. The input is obtained through a linear transformation:

$$\tilde{X}' = \text{Linear}(\tilde{X}) \in \mathbb{R}^{D \times H \times W}. \quad (15)$$

Referring to Equation 12, we can decompose the spectral components of the input filtered by the depthwise convolution:

$$\text{Conv}_{m \times m}(\tilde{X}'_d) = U f(\Lambda) \hat{X}'_d = \sum_{n=1}^{HW} f(\lambda_n) \hat{x}'_{dn} \mathbf{u}_n \quad (16)$$

where $\text{Conv}_{m \times m}(\cdot)$ is the $m \times m$ depthwise convolution, $\hat{X}'_d = U^T X'_d \in \mathbb{R}^{HW}$ denotes the GFT, $\hat{x}'_{dn} \in \mathbb{R}$ is its element, $f(\Lambda)$ is a diagonal matrix defining the filter function, $f(\lambda_n) \in \mathbb{R}$ is its element, and \mathbf{u}_n is a column vector of U . Since \mathbf{u}_n is the Fourier basis in GFT, we can say that convolution scales and aggregates spectral components. However, as shown in Figure 1, fixed-size convolution constrains spectral modulation based on kernel size. To address this, we assign different kernel sizes to each head.

The use of multiple kernels is a widely adopted design [83], [84]. To enhance adaptability, we introduce the *spectral re-scaling filter* (SRF), which refines the filtered spectrum using learnable parameters. This modification is applied to Equation 16 as follows:

$$\text{SRF}(\text{Conv}_{m \times m}(\tilde{X}'_d)) = \sum_{n=1}^{HW} \psi_n f(\lambda_n) \hat{x}'_{dn} \mathbf{u}_n, \quad (17)$$

where ψ_n is a learnable parameter constrained to the range $[0, 1]$. In 2D grid graphs (images) with periodic boundaries, the graph Laplacian eigenvectors align with the classical 2D discrete Fourier basis, differing only in basis ordering [85], [86]. Since our focus is solely on scaling each spectral component, we reformulate Equation 17 as a mask filtering problem in the 2D FFT to enable efficient implementation using `torch.fft.fft2`:

$$\text{SRF}(\text{Conv}_{m \times m}(\tilde{X}'_d)) = \mathcal{D}^{-1}(\Psi \odot \mathcal{D}(\text{Conv}_{m \times m}(\tilde{X}'_d))), \quad (18a)$$

$$\Psi = \phi(M), \quad (18b)$$

where \mathcal{D} and \mathcal{D}^{-1} denote the FFT and its inverse, respectively. Ψ is a re-scaling mask defined by a learnable mask M , which has the same shape as $\mathcal{D}(\text{Conv}_{m \times m}(\tilde{X}'_d))$. The function $\phi(\cdot)$ represents the sigmoid activation, ensuring values remain within the range $[0, 1]$.

Next, to enhance the representational capacity, we apply a linear expansion (Exp) that doubles the feature dimensions of SRF results. Specifically, the first head is computed as:

$$\text{Head}_1 = \text{Exp}(\text{SRF}(\text{Conv}_{m \times m}(\tilde{X}'_{:d_h}))), \quad (19)$$

where $\text{Head}_1 \in \mathbb{R}^{2d_h \times H \times W}$ and $\tilde{X}'_{:d_h} \in \mathbb{R}^{d_h \times H \times W}$ represents the input for this head. The same operation is applied to the remaining heads. Finally, all heads are concatenated along the feature dimension, followed by normalization and an activation function. A linear projection (Proj) then restores the feature dimensions to match \tilde{X} , yielding the spectral-adaptive context aggregation $\mathcal{C}(\cdot)$:

$$\mathcal{C}(\tilde{X}) = \text{Proj}(\sigma(\text{Norm}([\text{Head}_1; \text{Head}_2; \dots; \text{Head}_N])), \quad (20)$$

where $[\cdot; \cdot]$ denotes concatenation along the feature dimension, $\text{Norm}(\cdot)$ represents a normalization function, and $\mathcal{C}(\tilde{X}) \in \mathbb{R}^{D \times H \times W}$ is the final aggregated output.

TABLE I
ARCHITECTURE CONFIGURATIONS FOR SPANetV2.

Model size	Embedding dimensions	Block numbers	Activation
S18	[64, 128, 320, 512]	[3, 3, 9, 3]	GELU
S36	[64, 128, 320, 512]	[3, 12, 18, 3]	GELU
M36	[96, 192, 384, 576]	[3, 12, 18, 3]	GELU
B36	[128, 256, 512, 768]	[3, 12, 18, 3]	GELU

Note: All models adopt the Metaformer framework [45] for downsampling, using [7,3,3,3] kernels, [4,2,2,2] strides, and [2,1,1,1] padding at each stage.

C. The Spectral-Adaptive Modulation (SPAM) Mixer

Building on Equation 13, we introduce SPAM, a novel token mixer that utilizes $\mathcal{V}(\cdot)$ and $\mathcal{C}(\cdot)$, as illustrated in Figure 2. In SAG, we set $N = 4$ and assign kernel sizes of $[3, 5, 7, 9]$ to each head. GELU activation [87] is used for $\sigma(\cdot)$. To ensure stable training under our limited GPU resources, we apply a modified layer normalization for $\text{Norm}(\cdot)$, which can be implemented via PyTorch’s GroupNorm API [88] with a group size of 1, normalizing the spatial dimension [71]. Finally, after modulating $\mathcal{V}(\cdot)$ with $\mathcal{C}(\cdot)$, a linear transformation is applied to facilitate feature interaction, formulated as:

$$\text{SPAM}(\tilde{X}) = \text{Linear}(\mathcal{V}(\tilde{X}) \odot \mathcal{C}(\tilde{X})). \quad (21)$$

D. SPANetV2 Architectures

We introduce SPANetV2, a novel vision architecture that integrates the SPAM mixer within a four-stage hierarchical design, following the MetaFormer framework and its configurations [45]. SPANetV2 consists of two model variants: pure models, which utilize a uniform token mixer, and hybrid models, which incorporate heterogeneous mixers.

1) *Pure design*: Pure models follow all MetaFormer configurations, except replacing the token mixer with our SPAM and adopting GELU activation. Table I details the embedding dimensions and block numbers for each model size.

2) *Hybrid design*: In hybrid settings, the first two stages employ SPAM, while the latter two stages incorporate heterogeneous mixers such as self-attention or else [34], [45]. To further enhance the spectral capabilities of self-attention, we integrate attention features with convolutional features through element-wise addition, defined as follows:

$$\text{MixAttention}(X) = E(V) + \text{Conv}_{m \times m}(\tilde{V}), \quad (22a)$$

$$V = X^T W_v, \quad (22b)$$

where $\tilde{V} \in \mathbb{R}^{D \times H \times W}$ is obtained by reshaping V along the spatial dimensions, and $m = 7$. The detailed application is shown in Table V. This mixed attention improves convergence and enhances overall performance. In the following section, we evaluate SPANetV2 on ImageNet-1K classification—often associated with texture bias—and on several downstream tasks (e.g., object detection, instance segmentation, and semantic segmentation), where shape cues tend to be more critical [20], [89].

V. EXPERIMENTS

Following established practices [33], [45], [46], [59], we conduct comprehensive experiments to evaluate the effectiveness of the proposed SPANetV2 across three tasks: image classification on ImageNet-1K [58], object detection and instance segmentation on COCO [59], and semantic segmentation on ADE20K [60]. We first compare the performance of the proposed SPANetV2 with previous state-of-the-art methods across all three tasks. Additionally, we present an ablation study to assess the impact of individual design components within the proposed architecture. All experiments are implemented using PyTorch [88] on an Ubuntu 22.04 system equipped with four NVIDIA RTX4090 GPUs.

A. Image Classification on ImageNet-1K

1) *Setup*: ImageNet-1K [58] is a widely cited benchmark in computer vision, comprising 1.28M training and 50K validation images across 1K classes. Following the MetaFormer baseline settings [45], all models are trained for 300 epochs at 224² resolution. Data augmentation and regularization include MixUp [92], CutMix [93], CutOut [94], RandAugment [95], Label Smoothing [96], and Stochastic Depth [97]. We do not use repeated augmentation [98], [99] and LayerScale [100], but ResScale [101] is applied in the last two stages to facilitate deep model training. We adopt AdamW [102], [103] optimizer with weight decay 0.05 and a peak learning rate of $lr = 1e^{-3} \times \frac{\text{batch size}}{1024}$ for pure models. In contrast, LAMB [104] optimizer is adopted and a peak learning rate is set to $lr = 2e^{-3} \times \frac{\text{batch size}}{1024}$ for hybrid models. All models are trained with a batch size of 4096. The number of warmup epochs is 5, and cosine schedule is used to decay the learning rate. Our implementation is based on PyTorch-image-models [105] and the MetaFormer baseline [45].

2) *Results*: Table II presents the ImageNet-1K classification performance of SPANetV2. Our models achieve superior top-1 accuracy across S18, S36, M36, and B36 configurations in both pure and hybrid settings, surpassing various token-mixing approaches. Specifically, SPANetV2-S18-pure outperforms other convolution-based networks, such as multi-size kernel convolutions like FocalNet-T (1.1%p) and InceptionNeXt-T (1.4%p), and large-kernel designs including SLaK-T (0.9%p) and Conv2Former-T (0.2%p). Furthermore, it surpasses LITv2-S (1.4%p), which employs an attention-based mixer for low- and high-frequency processing, and DFFormer-S18 (0.2%p), which utilizes an input-adaptive dynamic spectral filter. Finally, SPANetV2-S18-hybrid surpasses all models, outperforming even other hybrid variants, exceeding CAFormer-S18 (0.5%p) and CDFFormer-S18 (0.8%p). Similar results are also observed for S36, M36, and B36.

B. Object Detection and Instance Segmentation on COCO

1) *Setup*: We evaluate SPANetV2 on the COCO benchmark [59], which comprises 118K training (train2017) and 5K validation (val2017) images. SPANetV2 serves as the backbone for Mask R-CNN [106] and Cascade Mask R-CNN [107]. Backbones are initialized with ImageNet pre-

TABLE II
PERFORMANCE COMPARISON OF MODELS TRAINED ON IMAGENET-1K AT THE RESOLUTION OF 224².

Model	Mixing type	Params (M)	MACs (G)	Latency (ms)	Top-1 (%)
RSB-ResNet-50 [1], [38]	C	26	4.1	-	79.8
ConvNeXt-T [39]	C	29	4.5	56.2	82.1
FocalNet-T (LRF) [83]	C	29	4.5	76.9	82.3
SPANet-S [57]	C	29	4.6	127.6	83.1
SLaK-T [41]	C	30	5.0	-	82.5
InceptionNeXt-T [84]	C	28	4.2	53.3	82.3
Conv2Former-T [42]	C	27	4.4	-	83.2
RDNet-T [90]	C	24	5.1	70.9	82.8
ConvFormer-S18 † [45]	C	27	3.9	84.0	83.0
SPANetV2-S18-pure (ours)	C	29	4.2	103.0	83.4
DeiT-S [6]	A	22	4.6	31.0	79.8
SwIn-T [8]	A	29	4.5	65.0	81.3
LITv2-S [81]	A	28	3.7	-	82.0
CSWin-T [26]	A	23	4.3	-	82.7
PoolFormerV2-S24 [45]	P	21	3.4	86.7	80.7
DFFormer-S18 † [34]	F	30	3.8	129.0	83.2
UniFormer-S [46]	CA	22	3.6	-	82.9
CAFormer-S18 † [45]	CA	26	4.1	92.1	83.4
CDFFormer-S18 † [34]	CF	30	3.9	105.3	83.1
SPANetV2-S18-hybrid (ours)	CA	27	4.2	104.9	83.9
RSB-ResNet-101 [1], [38]	C	45	7.9	-	81.3
ConvNeXt-S [39]	C	50	8.7	89.5	83.1
FocalNet-S (LRF) [83]	C	50	8.7	120.5	83.5
SPANet-M [57]	C	42	6.8	190.7	83.5
SLaK-S [41]	C	55	9.8	-	83.8
InceptionNeXt-S [84]	C	49	8.4	88.2	83.5
Conv2Former-S [42]	C	50	8.7	-	84.1
RDNet-S [90]	C	50	8.7	103.1	83.7
ConvFormer-S36 † [45]	C	40	7.6	158.9	84.1
SPANetV2-S36-pure (ours)	C	44	8.1	198.4	84.4
SwIn-S [8]	A	50	8.7	104.4	83.0
LITv2-M [81]	A	49	7.5	-	83.3
CSWin-S [26]	A	35	6.9	-	83.6
PoolFormerV2-S36 [45]	P	31	5.0	127.9	81.6
GFNet-H-S++ [33]	F	37	4.6	-	82.5
DFFormer-S36 † [34]	F	46	7.4	247.8	84.3
UniFormer-B [46]	CA	50	8.3	-	83.9
CAFormer-S36 † [45]	CA	39	8.0	174.9	84.4
CDFFormer-S36 † [34]	CF	45	7.5	200.0	84.2
SPANetV2-S36-hybrid (ours)	CA	41	8.1	203.1	84.7
RSB-ResNet-152 [1], [38]	C	60	11.6	-	81.8
RepLkNet-31B [40]	C	79	15.3	-	83.5
ConvNeXt-B [39]	C	89	15.4	133.3	83.8
FocalNet-B (LRF) [83]	C	89	15.4	179.5	83.9
SPANet-B [57]	C	76	12.0	293.2	84.0
SLaK-B [41]	C	95	15.4	-	84.0
InceptionNeXt-B [84]	C	87	14.9	133.0	84.0
Conv2Former-B [42]	C	90	15.9	-	84.4
RDNet-B [90]	C	88	15.4	154.0	84.4
ConvFormer-M36 † [45]	C	57	12.8	224.1	84.5
SPANetV2-M36-pure (ours)	C	61	13.7	276.4	84.9
DeiT-B [6]	A	86	17.5	86.4	81.8
SwIn-B [8]	A	88	15.4	153.4	83.5
LITv2-B [81]	A	87	13.2	-	83.6
CSWin-B [26]	A	78	15.0	-	84.2
MaxViT-S [91]	A	69	11.7	223.6	84.5
PoolFormerV2-M36 [45]	P	56	8.8	191.0	82.2
GFNet-H-B++ [33]	F	62	8.6	-	83.5
DFFormer-M36 † [34]	F	65	12.5	358.7	84.6
CAFormer-M36 † [45]	CA	56	13.2	242.9	85.1
CDFFormer-M36 † [34]	CF	64	12.7	287.0	84.8
SPANetV2-M36-hybrid (ours)	CA	58	13.6	278.8	85.3
ConvNeXt-L [39]	C	198	34.4	237.1	84.3
RDNet-L [90]	C	186	34.7	266.1	84.8
ConvFormer-B36 [45]	C	100	22.6	314.6	84.8
SPANetV2-B36-pure (ours)	C	100	24.3	395.4	85.0
MaxViT-B [91]	A	120	23.4	388.9	85.0
PoolFormerV2-M48 [45]	P	73	11.5	252.3	82.6
GFNet-H-L++ [33]	F	110	15.3	-	83.9
DFFormer-B36 [34]	F	115	22.1	500.0	84.8
CAFormer-B36 [45]	CA	99	23.2	339.3	85.5
CDFFormer-B36 [34]	CF	113	22.5	405.3	85.0
SPANetV2-B36-hybrid (ours)	CA	100	23.9	398.5	85.6

Note: The symbol '†' indicates models pretrained from scratch. The full names of the mixing types are as follows. C denotes Convolution, A denotes Attention, P denotes Pooling, F denotes FFT, CA represents a hybrid of Convolution and Attention, and CF represents a hybrid of Convolution and FFT. The inference time (ms) is measured for 128 images of size 224 × 224 on a RTX4090.

TABLE III
PERFORMANCE OF OBJECT DETECTION WITH MASK R-CNN AND CASCADE MASK R-CNN ON COCO VAL2017.

Backbone	MACs (G)	AP^b	AP_{50}^b	AP_{75}^b	AP^m	AP_{50}^m	AP_{75}^m
Mask R-CNN 3×							
Swin-T [8]	267	46.0	68.1	50.3	41.6	65.1	44.9
ConvNeXt-T [39]	262	46.2	67.9	50.8	41.7	65.0	44.9
Conv2Former-T [42]	-	48.0	69.5	52.7	43.0	66.8	46.1
RDNet-T [90]	278	47.5	68.5	52.1	42.4	65.6	45.7
ConvFormer-S18 [45]	251	47.7	69.6	52.3	42.6	66.3	45.9
SPANetV2-S18-pure (ours)	255	48.0	69.7	52.8	42.9	66.7	46.2
CAFormer-S18 [45]	254	48.6	70.5	53.4	43.7	67.5	47.4
SPANetV2-S18-hybrid (ours)	251	49.6	71.3	54.8	44.3	68.3	48.1
Cascade Mask R-CNN 3×							
Swin-T [8]	745	50.4	69.2	54.7	43.7	66.6	47.3
ConvNeXt-T [39]	741	50.4	69.1	54.8	43.7	66.5	47.3
SLaK-T [41]	-	51.3	70.0	55.7	44.3	67.2	48.1
Conv2Former-T [42]	-	51.4	69.8	55.9	44.5	67.4	48.3
ConvFormer-S18 [45]	729	51.5	70.7	55.8	44.6	67.8	48.2
SPANetV2-S18-pure (ours)	734	51.6	70.3	55.9	44.7	68.0	48.1
CAFormer-S18 [45]	733	52.3	71.3	56.9	45.2	68.6	48.8
SPANetV2-S18-hybrid (ours)	729	52.8	71.4	57.5	45.7	68.9	49.5

Note: The MACs are measured at a resolution of 1280×800 . Performance is reported in terms of bounding box AP and mask AP, denoted by AP^b and AP^m , respectively.

trained weights, while added layers use Xavier initialization [108]. Following ConvNeXt-based settings [39], models are trained for 36 epochs ($3 \times$ schedule) with a batch size of 16. AdamW [102], [103] is used with an initial learning rate of $1e^{-4}$ for Mask R-CNN and $2e^{-4}$ for Cascade Mask R-CNN. Training and testing images are resized to a shorter side of 800 pixels, with a maximum longer side of 1,333 pixels. Implementation is based on the `mm detection` [109] codebase.

2) *Results:* As shown in Table III, SPANetV2 models with Mask R-CNN [106] outperform their counterparts. SPANetV2-S18-pure achieves 48.0 AP^b and 42.9 AP^m , surpassing Swin-T (46.0 AP^b , 41.6 AP^m), ConvNeXt-T (46.2 AP^b , 41.7 AP^m), RDNet-T (47.5 AP^b , 42.4 AP^m), and ConvFormer-S18 (47.7 AP^b , 42.6 AP^m), while achieving comparable performance to Conv2Former-T (48.0 AP^b , 43.0 AP^m). Meanwhile, SPANetV2-S18-hybrid outperforms all models, attaining 49.6 AP^b and 44.3 AP^m , exceeding the hybrid model CAFormer-S18 (48.6 AP^b , 43.7 AP^m). Furthermore, SPANetV2-S18-pure with Cascade Mask R-CNN [107] surpasses all pure models, while SPANetV2-S18-hybrid outperforms all models, including CAFormer-S18. Due to our resource constraints, only S18 models are evaluated.

C. Semantic Segmentation on ADE20K

1) *Setup:* We also evaluate SPANetV2 on the ADE20K [60] for semantic segmentation, using 20K training and 2K validation images across 150 categories. We employ UperNet [110] and Semantic FPN [111] as semantic segmentation models, using `mm segmentation` [112] as the base framework with SPANetV2 as the backbone. Backbones are initialized with ImageNet-1K pre-trained weights, while newly added layers are initialized using Xavier initialization [108]. For UperNet training, we follow the ConvNeXt-based settings [39], training for 160K iterations with a batch size of 16, using the AdamW optimizer [102], [103] with an initial learning rate of $1e^{-4}$. For Semantic FPN, we adopt the PoolFormer-based settings [71], training for 40K iterations with a batch size of 32, using AdamW with an initial learning rate of $2e^{-4}$. Training images

TABLE IV
PERFORMANCE OF SEMANTIC SEGMENTATION WITH UPERNET AND SEMANTIC FPN ON ADE20K.

Backbone	Params (M)	MACs (G)	mIoU (%)
UperNet			
Swin-T [8]	60	945	45.8
ConvNeXt-T [39]	60	939	46.7
Conv2Former-T [42]	56	-	48.0
ConvFormer-S18 [45]	54	925	48.6
SPANetV2-S18-pure (ours)	60	930	48.7
CAFormer-S18 [45]	54	1024	48.9
SPANetV2-S18-hybrid (ours)	58	925	49.1
Swin-S [8]	81	1038	49.5
ConvNeXt-S [39]	82	1027	49.6
Conv2Former-S [42]	79	-	50.3
ConvFormer-S36 [45]	67	1003	50.7
SPANetV2-S36-pure (ours)	75	1012	49.8
CAFormer-S36 [45]	67	1197	50.8
SPANetV2-S36-hybrid (ours)	71	1004	51.6
Semantic FPN			
ResNet-50 [1]	29	46	36.7
Swin-T [8]	32	46	41.5
PoolFormer-S24 [71]	23	-	40.3
LITv2-S [81]	31	41	44.3
SPANet-S [57]	32	46	45.4
InceptionNeXt-T [84]	28	44	43.1
DFFormer-S18 [34]	32	-	45.1
SPANetV2-S18-pure (ours)	33	43	46.7
CDFFormer-S18 [34]	31	-	44.9
SPANetV2-S18-hybrid (ours)	31	48	47.8
ResNet-101 [1]	48	65	38.8
Swin-S [8]	53	70	45.2
PoolFormer-S36 [71]	35	-	42.0
LITv2-S [81]	52	63	45.7
SPANet-M [57]	45	57	46.2
InceptionNeXt-S [84]	50	65	45.6
DFFormer-S36 [34]	47	-	47.5
SPANetV2-S36-pure (ours)	48	64	47.9
CDFFormer-S36 [34]	47	-	46.7
SPANetV2-S36-hybrid (ours)	45	74	48.6

Note: The MACs are measured at a resolution of 512×2048 for UperNet and 512×512 for Semantic FPN, respectively.

are randomly resized and cropped to 512×512 , while testing images are rescaled to a shorter side of 512 pixels.

2) *Results:* As shown in Table IV, SPANetV2 with UperNet [110] outperforms existing models. Specifically, SPANetV2-S18-pure achieves 48.7% mIoU, surpassing all pure models, while SPANetV2-S18-hybrid attains 49.1%, outperforming all models, including the hybrid CAFormer-S18. For S36 models, SPANetV2-S36-pure achieves 49.8% mIoU with a marginal improvement, whereas SPANetV2-S36-hybrid sets a new state-of-the-art by reaching 51.2% mIoU. Similarly, SPANetV2 integrated with Semantic FPN [111] consistently outperforms prior models in semantic segmentation. SPANetV2-S18-pure achieves 46.7% mIoU, surpassing all pure models, while SPANetV2-S18-hybrid attains 47.8%, outperforming all models, including the hybrid CDFFormer-S18. Comparable trends are also observed in S36 models.

D. Ablation

This section presents ablation studies on SPANetV2-S18 using ImageNet-1K [58]. The results, summarized in Table V, are analyzed below across key aspects.

TABLE V
ABLATION FOR SPANetV2-S18 ON IMAGENET-1K.

Ablation	Variant	Top-1 (%)
-	SPANetV2-S18-pure	83.4
SPAM components	SAG with depth-wise SRF	
	→ without SRF	83.2 (-0.2)
	→ with a single SRF	83.4 (+0.0)
Hybrid stages	[SPAM, SPAM, SPAM, SPAM]	
	→ [SepConv, SepConv, SepConv, SepConv]	83.0 (-0.4)
	→ [SepConv, SepConv, SPAM, SPAM]	83.1 (-0.3)
	→ [SPAM, SPAM, Attention, Attention]	83.7 (+0.3)
	→ [SPAM, SPAM, MixAttention, MixAttention]	83.6 (+0.2)
	→ [SPAM, SPAM, MixAttention, Attention]	83.9 (+0.5)
Branch output scaling	ResScale [101]	
	→ None	83.2 (-0.2)
	→ LayerScale [100]	83.3 (-0.1)
	→ BranchScale [45]	83.3 (-0.1)
Biases in each block	Disable biases of Norm, FC and Conv → Enable biases	83.3 (-0.1)

Note: SepConv is employed in ConvFormer-S18 [45].

1) *SPAM components*: To assess the significance of SPAM components, we conduct experiments by modifying its operators. First, SRF is identified as a critical element of SAG, as its removal leads to a performance drop of -0.2% . Next, we configure SAG with a single SRF shared across all features in each head, achieving results identical to depth-wise SRF applied per feature dimension. However, using a single SRF reduces training stability as model size increases. Consequently, we employ depth-wise SRF for all SPANetV2 variants.

2) *Hybrid stages*: We evaluate SPAM-based token mixers by comparing different stacking strategies, including SepConv, Attention, and MixAttention. As shown in Table V, a uniform stacking of SPAM yields superior results compared to using only SepConv, highlighting the significance of spectral-adaptive convolution in enhancing model performance. Incorporating SPAM in the bottom two stages further improves performance over the SepConv-only configuration.

Next, we assess the impact of Attention and MixAttention in the bottom stages. Utilizing only Attention, as in CAFormer [45], improves SPANetV2-S18 performance by 0.3% , outperforming the configuration that solely employs MixAttention. However, combining MixAttention in the third stage with Attention in the final stage yields the highest improvement of 0.5% . Based on these findings, we adopt this configuration for all hybrid models.

3) *Branch output scaling*: Branch output scaling is evaluated based on the MetaFormer block, revealing that ResScale [101] is the most effective for SPANetV2. Notably, employing LayerScale [100] or combining both techniques [45] leads to a performance drop of -0.1% , while omitting scaling entirely further degrades performance by -0.2% .

4) *Biases in each block*: Enabling biases in each block results in a performance drop of -0.1% . This finding aligns with Yu *et al.* [45]. Consequently, we disable biases by default for all SPANetV2 models, following prior studies [113], [114].

VI. COMPARISON ANALYSIS

We analyze the feature representations of SPANetV2 and other MetaFormer-based models listed in Table II, includ-

ing ConvFormer, CAFormer [45], DFFormer, and CDFFormer [34]. While maintaining identical architectural configurations, these models only differ in their token mixers, such as SepConv, Attention, and Dynamic Filter, allowing for a fair comparison of their spectral filtering capabilities.

A. Relative Log Amplitude Analysis

Figure 3 depicts the relative log amplitudes of Fourier transformed features in different blocks for each token mixer. Across all models, high-frequency components remain less constrained (*i.e.*, shallow slope) in the lower layers (bright yellow curves) but undergo increasing suppression (*i.e.*, steep slope) in deeper layers (dense purple curves), leading to a bias toward low-frequency components. Notable differences arise in the middle layers: ConvFormer-S18 shows a gradual decline in high-frequency components, whereas DFFormer-S18 applies mild suppression, slightly attenuating high frequencies. In contrast, CAFormer-S18 and CDFFormer-S18 exhibit an opposite trend. Meanwhile, SPANet-S18-pure and -hybrid demonstrate larger fluctuations in the middle layers, suggesting more adaptive spectral modulation across stages. These findings indicate that token mixers with optimal flexibility in spectral adaptation can enhance vision model performance.

B. Models on Texture and Shape Bias

Previous studies suggest that spectral components encode fine details and global structures [72]–[74], related to texture and shape bias [54], [82]. To evaluate them, we utilize the modelvshuman toolbox [115], with results presented in Figure 4. The figure illustrates texture–shape bias across various models and human responses, illustrating the extent to which each model depends on texture versus shape cues for recognition. Despite pretraining on ImageNet-1K classification with identical augmentations as the Metaformer baseline [45], models exhibit distinct trends based on their token mixer types. For instance, DFFormer-S18 and CDFFormer-S18, which employ an input-adaptive FFT-based dynamic filter, demonstrate stronger shape bias than ConvFormer-S18 and CAFormer-S18. SPANetV2 models demonstrate comparable texture–shape bias to DFFormer-S18 and CDFFormer-S18, suggesting similar spectral filtering capabilities. However, as shown in Figure 3, SPANetV2 exhibits superior spectral adaptability. Notably, as illustrated in the boxplot below, SPANetV2-S18-hybrid shows a wider min-max range in shape bias than SPANetV2-S18-pure, indicating greater flexibility in spectral adaptation. This adaptability translates into state-of-the-art performance on ImageNet-1K classification and multiple downstream tasks (*i.e.*, object detection, instance segmentation, and semantic segmentation). These findings further highlight the importance of developing spectral-adaptive token mixers to optimize texture-shape bias and improve vision model performance.

VII. CONCLUSION

A. Discussion

In this paper, we conduct a theoretical analysis of the spectral properties of 2D convolution and self-attention through

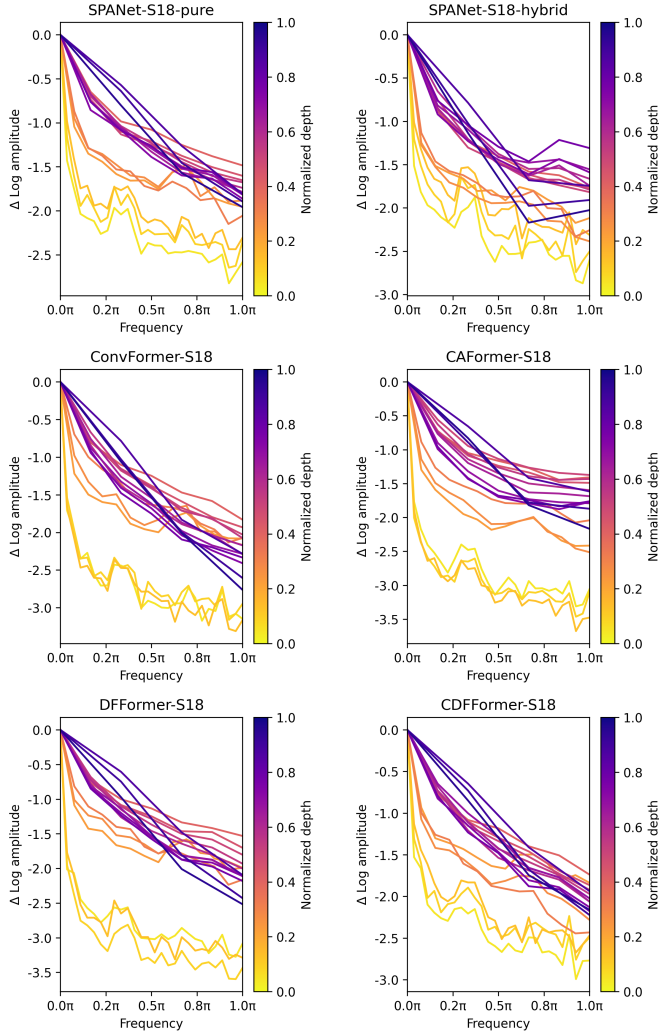


Fig. 3. **Relative log amplitudes of Fourier transformed feature maps on all stages.** All models follow the MetaFormer baseline [45] with configurations identical to Table I, except for the token mixers and activations.

graph spectral analysis. We identify node connectivity, modulated by window size, as a key factor in differentiating their spectral characteristics. Our findings align with prior studies, confirming that self-attention primarily exhibits low-pass filtering behavior, whereas convolution is more effective at capturing mid-/high-frequency components. Additionally, we discuss that larger kernels function as low-pass filters, providing insights into why they favor shape bias—corresponding to low-frequency components that encode shape information [40], [82].

Building on these insights, we propose SPAM, a novel token mixer designed to capture visual features in a spectral-adaptive manner. Specifically, we employ multiple kernels to extract diverse spectral components. Furthermore, inspired by the spectral analysis of 2D convolution, we introduce SRF, a spectral re-scaling filter that adjusts spectral components filtered by convolution. To achieve this, we reformulate the scaling problem as a mask filtering problem using the 2D FFT. With SPAM, we develop a series of SPANetV2 models and evaluate

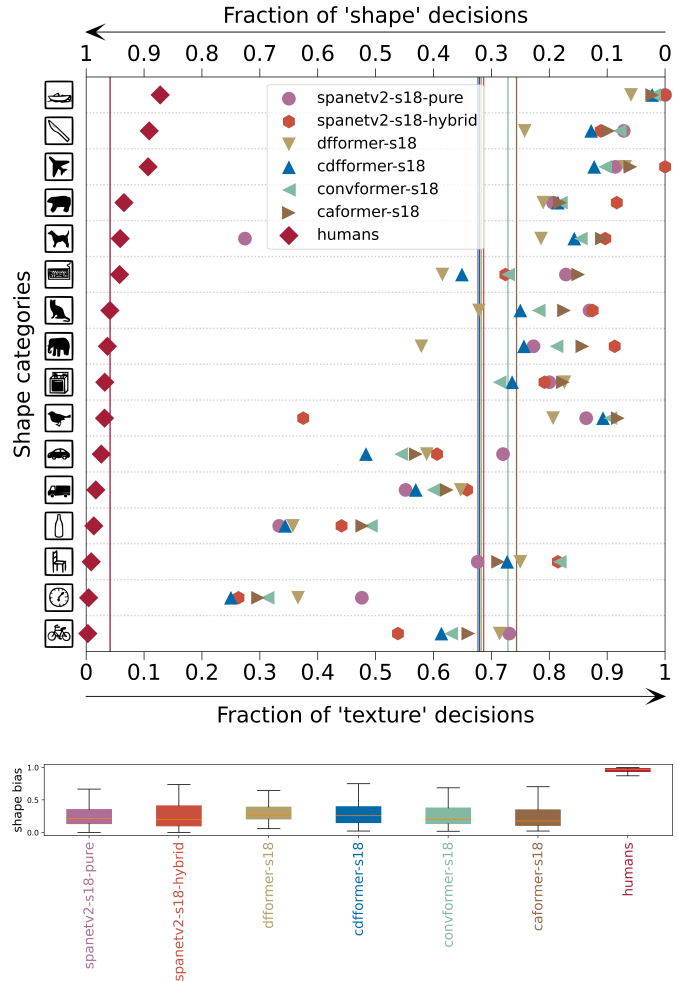


Fig. 4. **Evaluation of models on texture and shape bias.** All models are pretrained on ImageNet-1K classification using the same augmentations as the MetaFormer baseline [45].

them across three vision tasks, addressing both texture and shape bias. Experimental results demonstrate that SPANetV2 outperforms state-of-the-art models based on convolution, self-attention, and FFT in image classification, object detection and instance segmentation, and semantic segmentation.

B. Limitations

This study demonstrates that kernel size modulation of 2D convolution can induce spectral properties, and it shows large kernel convolutions are close to low-pass filters, akin to self-attention. However, it does not explain why optimizing larger kernels beyond 9×9 from scratch is more challenging than optimizing self-attention [40], [41]. In our experiments, SPAM is evaluated on a limited set of 2D vision tasks. Nonetheless, we believe spectral-adaptive approaches hold significant potential across diverse perception tasks, including audio, video, and 3D point cloud processing, which we leave for future work. Additionally, while SPAM enhances model performance with a marginal increase in parameters and MACs, its design is not optimized for inference efficiency. Future research should explore methods that balance spectral adaptation with computational efficiency.

ACKNOWLEDGMENTS

This work was supported by Samsung Research Funding & Incubation Center of Samsung Electronics under Project Number SRFC-IT2401-05.

REFERENCES

- [1] K. He, X. Zhang, S. Ren, and J. Sun, "Deep residual learning for image recognition," in *Proceedings of the IEEE conference on computer vision and pattern recognition*, 2016, pp. 770–778. **1, 2, 7, 8**
- [2] A. Krizhevsky, I. Sutskever, and G. E. Hinton, "Imagenet classification with deep convolutional neural networks," *Communications of the ACM*, vol. 60, no. 6, pp. 84–90, 2017. **1, 2**
- [3] K. Simonyan and A. Zisserman, "Very deep convolutional networks for large-scale image recognition," *arXiv preprint arXiv:1409.1556*, 2014. **1, 2**
- [4] C. Szegedy, W. Liu, Y. Jia, P. Sermanet, S. Reed, D. Anguelov, D. Erhan, V. Vanhoucke, and A. Rabinovich, "Going deeper with convolutions," in *Proceedings of the IEEE conference on computer vision and pattern recognition*, 2015, pp. 1–9. **1, 2**
- [5] A. Dosovitskiy, L. Beyer, A. Kolesnikov, D. Weissenborn, X. Zhai, T. Unterthiner, M. Dehghani, M. Minderer, G. Heigold, S. Gelly, J. Uszkoreit, and N. Houlsby, "An image is worth 16x16 words: Transformers for image recognition at scale," in *ICLR*, 2021. **1, 2, 4, 5**
- [6] H. Touvron, M. Cord, M. Douze, F. Massa, A. Sablayrolles, and H. Jégou, "Training data-efficient image transformers & distillation through attention," in *International conference on machine learning*. PMLR, 2021, pp. 10347–10357. **1, 7**
- [7] H. Wu, B. Xiao, N. Codella, M. Liu, X. Dai, L. Yuan, and L. Zhang, "Cvt: Introducing convolutions to vision transformers," in *Proceedings of the IEEE/CVF International Conference on Computer Vision*, 2021, pp. 22–31. **1, 2**
- [8] Z. Liu, Y. Lin, Y. Cao, H. Hu, Y. Wei, Z. Zhang, S. Lin, and B. Guo, "Swin transformer: Hierarchical vision transformer using shifted windows," in *Proceedings of the IEEE/CVF international conference on computer vision*, 2021, pp. 10012–10022. **1, 2, 5, 7, 8**
- [9] A. Vaswani, P. Ramachandran, A. Srinivas, N. Parmar, B. Hechtman, and J. Shlens, "Scaling local self-attention for parameter efficient visual backbones," in *Proceedings of the IEEE/CVF Conference on Computer Vision and Pattern Recognition*, 2021, pp. 12894–12904. **1**
- [10] N. Carion, F. Massa, G. Synnaeve, N. Usunier, A. Kirillov, and S. Zagoruyko, "End-to-end object detection with transformers," in *Computer Vision—ECCV 2020: 16th European Conference, Glasgow, UK, August 23–28, 2020, Proceedings, Part 1 16*. Springer, 2020, pp. 213–229. **1**
- [11] X. Zhu, W. Su, L. Lu, B. Li, X. Wang, and J. Dai, "Deformable detr: Deformable transformers for end-to-end object detection," in *ICLR*, 2021. **1**
- [12] M. Zheng, P. Gao, R. Zhang, K. Li, X. Wang, H. Li, and H. Dong, "End-to-end object detection with adaptive clustering transformer," in *arXiv preprint arXiv:2011.09315*, 2020. **1**
- [13] H. Wang, Y. Zhu, H. Adam, A. Yuille, and L.-C. Chen, "Max-deeplab: End-to-end panoptic segmentation with mask transformers," in *Proceedings of the IEEE/CVF conference on computer vision and pattern recognition*, 2021, pp. 5463–5474. **1**
- [14] Y. Wang, Z. Xu, X. Wang, C. Shen, B. Cheng, H. Shen, and H. Xia, "End-to-end video instance segmentation with transformers," in *Proc. IEEE Conf. Computer Vision and Pattern Recognition (CVPR)*, 2021. **1**
- [15] S. Chang, P. Wang, F. Wang, H. Li, and J. Feng, "Augmented transformer with adaptive graph for temporal action proposal generation," *arXiv preprint arXiv:2103.16024*, 2021. **1**
- [16] D. Neimark, O. Bar, M. Zohar, and D. Asselmann, "Video transformer network," in *Proceedings of the IEEE/CVF International Conference on Computer Vision*, 2021, pp. 3163–3172. **1**
- [17] N. Wang, W. Zhou, J. Wang, and H. Li, "Transformer meets tracker: Exploiting temporal context for robust visual tracking," in *Proceedings of the IEEE/CVF Conference on Computer Vision and Pattern Recognition*, 2021, pp. 1571–1580. **1**
- [18] D. Gong, J. Lee, M. Kim, S. J. Ha, and M. Cho, "Future transformer for long-term action anticipation," in *Proceedings of the IEEE/CVF Conference on Computer Vision and Pattern Recognition*, 2022, pp. 3052–3061. **1**
- [19] M. M. Naseer, K. Ranasinghe, S. H. Khan, M. Hayat, F. Shahbaz Khan, and M.-H. Yang, "Intriguing properties of vision transformers," in *NeurIPS*, 2021. **1**
- [20] S. Tuli, I. Dasgupta, E. Grant, and T. L. Griffiths, "Are convolutional neural networks or transformers more like human vision?" *arXiv preprint arXiv:2105.07197*, 2021. **1, 6**
- [21] T. Yu, X. Li, Y. Cai, M. Sun, and P. Li, "Rethinking token-mixing mlp for mlp-based vision backbone," *arXiv preprint arXiv:2106.14882*, 2021. **1**
- [22] X. Mao, G. Qi, Y. Chen, X. Li, R. Duan, S. Ye, Y. He, and H. Xue, "Towards robust vision transformer," in *Proceedings of the IEEE/CVF Conference on Computer Vision and Pattern Recognition*, 2022, pp. 12042–12051. **1**
- [23] X. Chu, Z. Tian, Y. Wang, B. Zhang, H. Ren, X. Wei, H. Xia, and C. Shen, "Twins: Revisiting the design of spatial attention in vision transformers," in *NeurIPS*, 2021. [Online]. Available: <https://openreview.net/forum?id=5kTIVBkzSRx> **1**
- [24] L. Yuan, Y. Chen, T. Wang, W. Yu, Y. Shi, Z.-H. Jiang, F. E. Tay, J. Feng, and S. Yan, "Tokens-to-token vit: Training vision transformers from scratch on imagenet," in *Proceedings of the IEEE/CVF international conference on computer vision*, 2021, pp. 558–567. **1**
- [25] W. Wang, E. Xie, X. Li, D.-P. Fan, K. Song, D. Liang, T. Lu, P. Luo, and L. Shao, "Pyramid vision transformer: A versatile backbone for dense prediction without convolutions," in *Proceedings of the IEEE/CVF international conference on computer vision*, 2021, pp. 568–578. **1**
- [26] X. Dong, J. Bao, D. Chen, W. Zhang, N. Yu, L. Yuan, D. Chen, and B. Guo, "Cswin transformer: A general vision transformer backbone with cross-shaped windows," in *Proceedings of the IEEE/CVF conference on computer vision and pattern recognition*, 2022, pp. 12124–12134. **1, 7**
- [27] I. Tolstikhin, N. Houlsby, A. Kolesnikov, L. Beyer, X. Zhai, T. Unterthiner, J. Yung, A. Steiner, D. Keysers, J. Uszkoreit, M. Lucic, and A. Dosovitskiy, "Mlp-mixer: An all-mlp architecture for vision," in *NeurIPS*, 2021. **1, 2**
- [28] Q. Hou, Z. Jiang, L. Yuan, M.-M. Cheng, S. Yan, and J. Feng, "Vision permutator: A permutable mlp-like architecture for visual recognition," in *IEEE Transactions on Pattern Analysis and Machine Intelligence*. IEEE, 2022. **1, 2**
- [29] H. Touvron, P. Bojanowski, M. Caron, M. Cord, A. El-Nouby, E. Grave, G. Izacard, A. Joulin, G. Synnaeve, J. Verbeek *et al.*, "Resmlp: Feed-forward networks for image classification with data-efficient training," in *IEEE Transactions on Pattern Analysis and Machine Intelligence*. IEEE, 2022. **1, 2**
- [30] Y. Tang, K. Han, J. Guo, C. Xu, Y. Li, C. Xu, and Y. Wang, "An image patch is a wave: Phase-aware vision mlp," in *CVPR*, 2022. **1**
- [31] S. Chen, E. Xie, C. Ge, R. Chen, D. Liang, and P. Luo, "Cyclemlp: a mlp-like architecture for dense visual predictions," *IEEE Transactions on Pattern Analysis and Machine Intelligence*, 2023. **1**
- [32] J. Lee-Thorp, J. Ainslie, I. Eckstein, and S. Ontanon, "FNet: Mixing tokens with Fourier transforms," in *Proceedings of the 2022 Conference of the North American Chapter of the Association for Computational Linguistics: Human Language Technologies*. Seattle, United States: Association for Computational Linguistics, Jul. 2022, pp. 4296–4313. [Online]. Available: <https://aclanthology.org/2022.naacl-main.319> **1, 2**
- [33] Y. Rao, W. Zhao, Z. Zhu, J. Zhou, and J. Lu, "Gfnet: Global filter networks for visual recognition," *IEEE Transactions on Pattern Analysis and Machine Intelligence*, vol. 45, no. 9, pp. 10960–10973, 2023. **1, 2, 7**
- [34] Y. Tatsunami and M. Taki, "Fft-based dynamic token mixer for vision," in *Proceedings of the AAAI Conference on Artificial Intelligence*, vol. 38, no. 14, 2024, pp. 15328–15336. **1, 2, 6, 7, 8, 9**
- [35] K. Han, Y. Wang, J. Guo, Y. Tang, and E. Wu, "Vision gnn: An image is worth graph of nodes," *Advances in neural information processing systems*, vol. 35, pp. 8291–8303, 2022. **1, 2**
- [36] X. Ma, Y. Zhou, H. Wang, C. Qin, B. Sun, C. Liu, and Y. Fu, "Image as set of points," in *The Eleventh International Conference on Learning Representations*, 2023. [Online]. Available: <https://openreview.net/forum?id=awnvqZja69> **1, 2**
- [37] J. Liang, Y. Cui, Q. Wang, T. Geng, W. Wang, and D. Liu, "Clusterformer: Clustering as a universal visual learner," *Advances in Neural Information Processing Systems*, vol. 36, 2023. **1, 2**
- [38] R. Wightman, H. Touvron, and H. Jégou, "Resnet strikes back: An improved training procedure in timm," *arXiv preprint arXiv:2110.00476*, 2021. **1, 7**
- [39] Z. Liu, H. Mao, C.-Y. Wu, C. Feichtenhofer, T. Darrell, and S. Xie, "A convnet for the 2020s," in *Proceedings of the IEEE/CVF conference*

- on computer vision and pattern recognition, 2022, pp. 11 976–11 986. **1, 7, 8**
- [40] X. Ding, X. Zhang, J. Han, and G. Ding, “Scaling up your kernels to 31x31: Revisiting large kernel design in cnns,” in *Proceedings of the IEEE/CVF conference on computer vision and pattern recognition*, 2022, pp. 11 963–11 975. **1, 2, 5, 7, 10**
- [41] S. Liu, T. Chen, X. Chen, X. Chen, Q. Xiao, B. Wu, T. Kärkkäinen, M. Pechenizkiy, D. Mocuano, and Z. Wang, “More convnets in the 2020s: Scaling up kernels beyond 51x51 using sparsity,” in *ICLR*, 2023. **1, 7, 8, 10**
- [42] Q. Hou, C.-Z. Lu, M.-M. Cheng, and J. Feng, “Conv2former: A simple transformer-style convnet for visual recognition,” *IEEE transactions on pattern analysis and machine intelligence*, 2024. **1, 5, 7, 8**
- [43] Y. Rao, W. Zhao, Y. Tang, J. Zhou, S. N. Lim, and J. Lu, “Hornet: Efficient high-order spatial interactions with recursive gated convolutions,” *Advances in Neural Information Processing Systems*, vol. 35, pp. 10 353–10 366, 2022. **1**
- [44] W. Wang, J. Dai, Z. Chen, Z. Huang, Z. Li, X. Zhu, X. Hu, T. Lu, L. Lu, H. Li *et al.*, “Internimage: Exploring large-scale vision foundation models with deformable convolutions,” in *Proceedings of the IEEE/CVF Conference on Computer Vision and Pattern Recognition*, 2023, pp. 14 408–14 419. **1**
- [45] W. Yu, C. Si, P. Zhou, M. Luo, Y. Zhou, J. Feng, S. Yan, and X. Wang, “Metaformer baselines for vision,” *IEEE Transactions on Pattern Analysis and Machine Intelligence*, 2024. **1, 2, 6, 7, 8, 9, 10**
- [46] K. Li, Y. Wang, J. Zhang, P. Gao, G. Song, Y. Liu, H. Li, and Y. Qiao, “Uniformer: Unifying convolution and self-attention for visual recognition,” *IEEE Transactions on Pattern Analysis and Machine Intelligence*, vol. 45, no. 10, pp. 12 581–12 600, 2023. **1, 7**
- [47] Z. Dai, H. Liu, Q. V. Le, and M. Tan, “Coatnet: Marrying convolution and attention for all data sizes,” *Advances in neural information processing systems*, vol. 34, pp. 3965–3977, 2021. **1**
- [48] Y. Zhao, G. Wang, C. Tang, C. Luo, W. Zeng, and Z.-J. Zha, “A battle of network structures: An empirical study of cnn, transformer, and mlp,” *arXiv preprint arXiv:2108.13002*, 2021. **1**
- [49] Q. Zhang, Y. Xu, J. Zhang, and D. Tao, “Vitaev2: Vision transformer advanced by exploring inductive bias for image recognition and beyond,” *International Journal of Computer Vision*, vol. 131, no. 5, pp. 1141–1162, 2023. **1**
- [50] Z. Pan, J. Cai, and B. Zhuang, “Fast vision transformers with hilo attention,” *Advances in Neural Information Processing Systems*, vol. 35, pp. 14 541–14 554, 2022. **1, 2**
- [51] N. Park and S. Kim, “How do vision transformers work?” in *International Conference on Learning Representations*, 2022. **1, 2, 5**
- [52] J. Bai, L. Yuan, S.-T. Xia, S. Yan, Z. Li, and W. Liu, “Improving vision transformers by revisiting high-frequency components,” in *European Conference on Computer Vision*. Springer, 2022, pp. 1–18. **1, 2, 5**
- [53] P. Wang, W. Zheng, T. Chen, and Z. Wang, “Anti-oversmoothing in deep vision transformers via the fourier domain analysis: From theory to practice,” in *International Conference on Learning Representations*, 2022. [Online]. Available: <https://openreview.net/forum?id=O476oWmiNNp> **1, 2, 5**
- [54] H. Wang, X. Wu, Z. Huang, and E. P. Xing, “High-frequency component helps explain the generalization of convolutional neural networks,” in *Proceedings of the IEEE/CVF conference on computer vision and pattern recognition*, 2020, pp. 8684–8694. **1, 2, 5, 9**
- [55] Z. Wang, H. Luo, P. Wang, F. Ding, F. Wang, and H. Li, “Vtc-lfc: Vision transformer compression with low-frequency components,” *Advances in Neural Information Processing Systems*, vol. 35, pp. 13 974–13 988, 2022. **1, 2, 5**
- [56] H. Chen, Y. Zhang, X. Feng, X. Chu, and K. Huang, “Revealing the dark secrets of extremely large kernel convnets on robustness,” in *International Conference on Machine Learning*. PMLR, 2024, pp. 7687–7699. **1, 2**
- [57] G. Yun, J. Yoo, K. Kim, J. Lee, and D. H. Kim, “Spanet: Frequency-balancing token mixer using spectral pooling aggregation modulation,” in *Proceedings of the IEEE/CVF International Conference on Computer Vision*, 2023, pp. 6113–6124. **2, 5, 7, 8**
- [58] J. Deng, W. Dong, R. Socher, L.-J. Li, K. Li, and L. Fei-Fei, “Imagenet: A large-scale hierarchical image database,” in *2009 IEEE conference on computer vision and pattern recognition*. Ieee, 2009, pp. 248–255. **2, 7, 8**
- [59] T.-Y. Lin, M. Maire, S. Belongie, J. Hays, P. Perona, D. Ramanan, P. Dollár, and C. L. Zitnick, “Microsoft coco: Common objects in context,” in *Computer Vision—ECCV 2014: 13th European Conference, Zurich, Switzerland, September 6–12, 2014, Proceedings, Part V 13*. Springer, 2014, pp. 740–755. **2, 7**
- [60] B. Zhou, H. Zhao, X. Puig, S. Fidler, A. Barriuso, and A. Torralba, “Scene parsing through ade20k dataset,” in *Proceedings of the IEEE conference on computer vision and pattern recognition*, 2017, pp. 633–641. **2, 7, 8**
- [61] A. Vaswani, N. Shazeer, N. Parmar, J. Uszkoreit, L. Jones, A. N. Gomez, Ł. Kaiser, and I. Polosukhin, “Attention is all you need,” in *Advances in neural information processing systems*, vol. 30, 2017. **2**
- [62] K. Wu, H. Peng, M. Chen, J. Fu, and H. Chao, “Rethinking and improving relative position encoding for vision transformer,” in *Proceedings of the IEEE/CVF International Conference on Computer Vision*, 2021, pp. 10 033–10 041. **2**
- [63] S. Qian, H. Shao, Y. Zhu, M. Li, and J. Jia, “Blending anti-aliasing into vision transformer,” in *NeurIPS*, 2021. **2**
- [64] S. d’Ascoli, H. Touvron, M. L. Leavitt, A. S. Morcos, G. Biroli, and L. Sagun, “Convit: Improving vision transformers with soft convolutional inductive biases,” in *International Conference on Machine Learning*. PMLR, 2021, pp. 2286–2296. **2**
- [65] J. Guo, K. Han, H. Wu, Y. Tang, X. Chen, Y. Wang, and C. Xu, “Cmt: Convolutional neural networks meet vision transformers,” in *Proceedings of the IEEE/CVF Conference on Computer Vision and Pattern Recognition*, 2022, pp. 12 175–12 185. **2**
- [66] S. Chen, E. Xie, C. GE, R. Chen, D. Liang, and P. Luo, “CycleMLP: A MLP-like architecture for dense prediction,” in *International Conference on Learning Representations*, 2022. [Online]. Available: <https://openreview.net/forum?id=NMEceG4v69Y> **2**
- [67] A. Martins, A. Farinhas, M. Tréviso, V. Niculae, P. Aguiar, and M. Figueiredo, “Sparse and continuous attention mechanisms,” in *NeurIPS*, 2020. **2**
- [68] P. H. Martins, Z. Marinho, and A. F. Martins, “∞-former: Infinite memory transformer,” in *Proc. ACL*, 2022. **2**
- [69] G. Wang, Y. Zhao, C. Tang, C. Luo, and W. Zeng, “When shift operation meets vision transformer: An extremely simple alternative to attention mechanism,” in *Proceedings of the AAAI Conference on Artificial Intelligence*, vol. 36, no. 2, 2022, pp. 2423–2430. **2**
- [70] J. Lin, C. Gan, and S. Han, “Tsm: Temporal shift module for efficient video understanding,” in *Proceedings of the IEEE/CVF international conference on computer vision*, 2019, pp. 7083–7093. **2**
- [71] W. Yu, M. Luo, P. Zhou, C. Si, Y. Zhou, X. Wang, J. Feng, and S. Yan, “Metaformer is actually what you need for vision,” in *Proceedings of the IEEE/CVF Conference on Computer Vision and Pattern Recognition*, 2022, pp. 10 819–10 829. **2, 6, 8**
- [72] Y. Chen, H. Fan, B. Xu, Z. Yan, Y. Kalantidis, M. Rohrbach, S. Yan, and J. Feng, “Drop an octave: Reducing spatial redundancy in convolutional neural networks with octave convolution,” in *Proceedings of the IEEE/CVF international conference on computer vision*, 2019, pp. 3435–3444. **2, 9**
- [73] J. W. Cooley, P. A. Lewis, and P. D. Welch, “The fast fourier transform and its applications,” *IEEE Transactions on Education*, vol. 12, no. 1, pp. 27–34, 1969. **2, 9**
- [74] G. Deng and L. Cahill, “An adaptive gaussian filter for noise reduction and edge detection,” in *1993 IEEE conference record nuclear science symposium and medical imaging conference*. IEEE, 1993, pp. 1615–1619. **2, 9**
- [75] Z. Huang, Z. Zhang, C. Lan, Z.-J. Zha, Y. Lu, and B. Guo, “Adaptive frequency filters as efficient global token mixers,” in *Proceedings of the IEEE/CVF International Conference on Computer Vision*, 2023, pp. 6049–6059. **2**
- [76] D. I. Shuman, S. K. Narang, P. Frossard, A. Ortega, and P. Vandergheynst, “The emerging field of signal processing on graphs: Extending high-dimensional data analysis to networks and other irregular domains,” *IEEE signal processing magazine*, vol. 30, no. 3, pp. 83–98, 2013. **2, 3**
- [77] M. Balcilar, G. Renton, P. Héroux, B. Gaüzère, S. Adam, and P. Honeine, “Analyzing the expressive power of graph neural networks in a spectral perspective,” in *International Conference on Learning Representations*, 2021. **2, 3, 5**
- [78] F. R. Chung, *Spectral graph theory*. American Mathematical Soc., 1997, vol. 92. **3**
- [79] B. Liu, M. Wang, H. Foroosh, M. Tappen, and M. Pensky, “Sparse convolutional neural networks,” in *Proceedings of the IEEE conference on computer vision and pattern recognition*, 2015, pp. 806–814. **3**
- [80] Y. Tan, K. Han, K. Zhao, X. Yu, Z. Du, Y. Chen, Y. Wang, and J. Yao, “Accelerating sparse convolution with column vector-wise sparsity,” *Advances in Neural Information Processing Systems*, vol. 35, pp. 30 307–30 317, 2022. **3**
- [81] Z. Pan, J. Cai, and B. Zhuang, “Fast vision transformers with hilo attention,” in *NeurIPS*, 2022. **5, 7, 8**

- [82] A. Subramanian, E. Sizikova, N. Majaj, and D. Pelli, "Spatial-frequency channels, shape bias, and adversarial robustness," *Advances in neural information processing systems*, vol. 36, pp. 4137–4149, 2023. [5](#), [9](#), [10](#)
- [83] J. Yang, C. Li, X. Dai, and J. Gao, "Focal modulation networks," *Advances in Neural Information Processing Systems*, vol. 35, pp. 4203–4217, 2022. [5](#), [6](#), [7](#)
- [84] W. Yu, P. Zhou, S. Yan, and X. Wang, "Inceptionnext: When inception meets convnext," in *Proceedings of the IEEE/CVF Conference on Computer Vision and Pattern Recognition*, 2024, pp. 5672–5683. [6](#), [7](#), [8](#)
- [85] V. N. Ekambaram, *Graph-structured data viewed through a Fourier lens*. University of California, Berkeley, 2014. [6](#)
- [86] V. N. Ekambaram, G. C. Fanti, B. Ayazifar, and K. Ramchandran, "Circulant structures and graph signal processing," in *2013 IEEE International Conference on Image Processing*. IEEE, 2013, pp. 834–838. [6](#)
- [87] D. Hendrycks and K. Gimpel, "Gaussian error linear units (gelus)," *arXiv preprint arXiv:1606.08415*, 2016. [6](#)
- [88] A. Paszke, S. Gross, F. Massa, A. Lerer, J. Bradbury, G. Chanan, T. Killeen, Z. Lin, N. Gimelshein, L. Antiga *et al.*, "Pytorch: An imperative style, high-performance deep learning library," *Advances in neural information processing systems*, vol. 32, 2019. [6](#), [7](#)
- [89] R. Geirhos, P. Rubisch, C. Michaelis, M. Bethge, F. A. Wichmann, and W. Brendel, "Imagenet-trained cnns are biased towards texture; increasing shape bias improves accuracy and robustness," in *International conference on learning representations*, 2019. [6](#)
- [90] D. Kim, B. Heo, and D. Han, "Densenets reloaded: paradigm shift beyond resnets and vits," in *European Conference on Computer Vision*. Springer, 2025, pp. 395–415. [7](#), [8](#)
- [91] Z. Tu, H. Talebi, H. Zhang, F. Yang, P. Milanfar, A. Bovik, and Y. Li, "Maxvit: Multi-axis vision transformer," in *European conference on computer vision*. Springer, 2022, pp. 459–479. [7](#)
- [92] H. Zhang, M. Cisse, Y. N. Dauphin, and D. Lopez-Paz, "mixup: Beyond empirical risk minimization," in *International Conference on Learning Representations*, 2018. [7](#)
- [93] S. Yun, D. Han, S. J. Oh, S. Chun, J. Choe, and Y. Yoo, "Cutmix: Regularization strategy to train strong classifiers with localizable features," in *Proceedings of the IEEE/CVF international conference on computer vision*, 2019, pp. 6023–6032. [7](#)
- [94] Z. Zhong, L. Zheng, G. Kang, S. Li, and Y. Yang, "Random erasing data augmentation," in *Proceedings of the AAAI conference on artificial intelligence*, vol. 34, no. 07, 2020, pp. 13 001–13 008. [7](#)
- [95] E. D. Cubuk, B. Zoph, J. Shlens, and Q. V. Le, "Randaugment: Practical automated data augmentation with a reduced search space," in *Proceedings of the IEEE/CVF conference on computer vision and pattern recognition workshops*, 2020, pp. 702–703. [7](#)
- [96] C. Szegedy, V. Vanhoucke, S. Ioffe, J. Shlens, and Z. Wojna, "Rethinking the inception architecture for computer vision," in *Proceedings of the IEEE conference on computer vision and pattern recognition*, 2016, pp. 2818–2826. [7](#)
- [97] G. Huang, Y. Sun, Z. Liu, D. Sedra, and K. Q. Weinberger, "Deep networks with stochastic depth," in *Computer Vision—ECCV 2016: 14th European Conference, Amsterdam, The Netherlands, October 11–14, 2016, Proceedings, Part IV 14*. Springer, 2016, pp. 646–661. [7](#)
- [98] M. Berman, H. Jégou, A. Vedaldi, I. Kokkinos, and M. Douze, "Multigrain: a unified image embedding for classes and instances," *arXiv preprint arXiv:1902.05509*, 2019. [7](#)
- [99] E. Hoffer, T. Ben-Nun, I. Hubara, N. Giladi, T. Hoeffler, and D. Soudry, "Augment your batch: Improving generalization through instance repetition," in *Proceedings of the IEEE/CVF Conference on Computer Vision and Pattern Recognition*, 2020, pp. 8129–8138. [7](#)
- [100] H. Touvron, M. Cord, A. Sablayrolles, G. Synnaeve, and H. Jégou, "Going deeper with image transformers," in *Proceedings of the IEEE/CVF International Conference on Computer Vision*, 2021, pp. 32–42. [7](#), [9](#)
- [101] S. Shleifer, J. Weston, and M. Ott, "Normformer: Improved transformer pretraining with extra normalization," *arXiv preprint arXiv:2110.09456*, 2021. [7](#), [9](#)
- [102] D. P. Kingma and J. Ba, "Adam: A method for stochastic optimization," *arXiv preprint arXiv:1412.6980*, 2014. [7](#), [8](#)
- [103] I. Loshchilov and F. Hutter, "Decoupled weight decay regularization," in *International Conference on Learning Representations*, 2019. [7](#), [8](#)
- [104] Y. You, J. Li, S. Reddi, J. Hseu, S. Kumar, S. Bhojanapalli, X. Song, J. Demmel, K. Keutzer, and C.-J. Hsieh, "Large batch optimization for deep learning: Training bert in 76 minutes," *arXiv preprint arXiv:1904.00962*, 2019. [7](#)
- [105] R. Wightman, "Pytorch image models," <https://github.com/rwightman/pytorch-image-models>, 2019. [7](#)
- [106] K. He, G. Gkioxari, P. Dollár, and R. Girshick, "Mask r-cnn," in *Proceedings of the IEEE international conference on computer vision*, 2017, pp. 2961–2969. [7](#), [8](#)
- [107] Z. Cai and N. Vasconcelos, "Cascade r-cnn: Delving into high quality object detection," in *Proceedings of the IEEE conference on computer vision and pattern recognition*, 2018, pp. 6154–6162. [7](#), [8](#)
- [108] X. Glorot and Y. Bengio, "Understanding the difficulty of training deep feedforward neural networks," in *Proceedings of the thirteenth international conference on artificial intelligence and statistics*. JMLR Workshop and Conference Proceedings, 2010, pp. 249–256. [8](#)
- [109] K. Chen, J. Wang, J. Pang, Y. Cao, Y. Xiong, X. Li, S. Sun, W. Feng, Z. Liu, J. Xu *et al.*, "Mmdetection: Open mmlab detection toolbox and benchmark," *arXiv preprint arXiv:1906.07155*, 2019. [8](#)
- [110] T. Xiao, Y. Liu, B. Zhou, Y. Jiang, and J. Sun, "Unified perceptual parsing for scene understanding," in *Proceedings of the European conference on computer vision (ECCV)*, 2018, pp. 418–434. [8](#)
- [111] A. Kirillov, R. Girshick, K. He, and P. Dollár, "Panoptic feature pyramid networks," in *Proceedings of the IEEE/CVF conference on computer vision and pattern recognition*, 2019, pp. 6399–6408. [8](#)
- [112] M. Contributors, "MMSegmentation: Openmmlab semantic segmentation toolbox and benchmark," <https://github.com/open-mmlab/mms Segmentation>, 2020. [8](#)
- [113] C. Raffel, N. Shazeer, A. Roberts, K. Lee, S. Narang, M. Matena, Y. Zhou, W. Li, and P. J. Liu, "Exploring the limits of transfer learning with a unified text-to-text transformer," *Journal of machine learning research*, vol. 21, no. 140, pp. 1–67, 2020. [9](#)
- [114] A. Chowdhery, S. Narang, J. Devlin, M. Bosma, G. Mishra, A. Roberts, P. Barham, H. W. Chung, C. Sutton, S. Gehrmann *et al.*, "Palm: Scaling language modeling with pathways," *Journal of Machine Learning Research*, vol. 24, no. 240, pp. 1–113, 2023. [9](#)
- [115] bethgelab, "Toolbox of model-vs-human," <https://github.com/bethgelab/model-vs-human>, 2021. [9](#)